

Charge-imbalance-induced second harmonic generation in twisted graphene

Ronghui Luo(罗荣辉), Shiyang Liu(刘诗洋), Xiao Dong(董校), Jianguo Tian(田建国), and Zhibo Liu(刘智波)
Citation: Chin. Phys. B, 2026, 35 (**3**): 034201. DOI: 10.1088/1674-1056/ae3557
http://cpb.iphy.ac.cn; http://iopscience.iop.org/cpb

What follows is a list of articles you may be interested in

Strain modulation of second harmonic generation in new tetrahedral transition metal dichalcogenide monolayers

Hu Chen(陈虎), Shi-Qi Li(李仕琪), Yuqing Wu(吴雨晴), Xiaozhendong Bao(鲍晓振东), Zhijie Lei(雷志杰), Hongsheng Liu(柳洪盛), Yuee Xie(谢月娥), Junfeng Gao(高峻峰), Yuanping Chen(陈元平), and Xiaohong Yan(颜晓红)
Chin. Phys. B, 2025, 34 (**8**): 084206. DOI: 10.1088/1674-1056/addaa3

Simultaneous second and third harmonics generation in periodically poled lithium niobate: Coupling and competition

Junming Liu(刘峻铭), Liqiang Liu(刘励强), Lihong Hong(洪丽红), and Zhiyuan Li(李志远)
Chin. Phys. B, 2025, 34 (**8**): 084203. DOI: 10.1088/1674-1056/add24a

Heterogeneous integration of silicon nitride photonics and CVD-grown WS_2 for second harmonic generation

Xuhang Jia(贾旭航), Bangren Xu(许邦仁), Jieyi Luo(罗劼舣), Ning Liu(刘宁), Yuhang Wang(王宇航), Biyuan Zheng(郑弼元), Wei Xu(徐威), and Ken Liu(刘肯)
Chin. Phys. B, 2025, 34 (**7**): 074205. DOI: 10.1088/1674-1056/adc7f7

A global model of intensity autocorrelation to determine laser pulse duration

Yufei Peng(彭雨菲), Liqiang Liu(刘励强), Lihong Hong(洪丽红), and Zhiyuan Li(李志远)
Chin. Phys. B, 2024, 33 (**5**): 054207. DOI: 10.1088/1674-1056/ad1c57

Second harmonic generation from precise diamond blade diced ridge waveguides

Hui Xu(徐慧), Ziqi Li(李子琦), Chi Pang(逄驰), Rang Li(李让), Genglin Li(李庚霖), Sh. Akhmadaliev, Shengqiang Zhou(周生强), Qingming Lu(路庆明), Yuechen Jia(贾曰辰), and Feng Chen(陈峰)
Chin. Phys. B, 2022, 31 (**9**): 094209. DOI: 10.1088/1674-1056/ac5242

RAPID COMMUNICATION

Charge-imbalance-induced second harmonic generation in twisted graphene

Ronghui Luo(罗荣辉)[1], Shiyang Liu(刘诗洋)[1], Xiao Dong(董校)[1], Jianguo Tian(田建国)[1], and Zhibo Liu(刘智波)[1,2,†]

[1] *The Key Laboratory of Weak Light Nonlinear Photonics, Ministry of Education, School of Physics and Teda Applied Physics Institute, Nankai University, Tianjin* 300071, *China*

[2] *The Collaborative Innovation Center of Extreme Optics, Shanxi University, Taiyuan* 030006, *China*

(Received 8 December 2025; revised manuscript received 26 December 2025; accepted manuscript online 8 January 2026)

Twist-and-stack engineering provides a programmable degree of freedom for nonlinear optics in two-dimensional materials, yet in a homostructure whose constituents have no second harmonic generation (SHG), how interlayer coupling grants and tunes second-order response remains unclear. Here, we use twisted monolayer-bilayer graphene ($t(1+2)$LG) and combine microscopic SHG spectroscopy with first-principles differential charge-density analysis to establish a unified "permission-and-resonance" mechanism. Interlayer coupling creates an interlayer charge imbalance within the AB-stacked bilayer, breaking inversion symmetry and thereby permitting an in-plane electric-dipole response. At the same time, the twist angle steers van Hove singularities in the band structure to achieve two-photon resonance, which markedly amplifies the susceptibility $\chi^{(2)}$. Experimentally, at $\theta = 13.5^\circ$, we obtain $\chi^{(2)} = 279.4$ pm/V, evidencing a highly efficient second-order response. These results identify SHG as a sensitive probe of interlayer coupling and charge redistribution in homostructure van der Waals systems.

Keywords: second harmonic generation, charge imbalance, twisted graphene

PACS: 42.65.Ky, 78.67.–n

DOI: 10.1088/1674-1056/ae3557 **CSTR:** 32038.14.CPB.ae3557

Van der Waals (vdW) layered materials form moiré superlattices under a controllable twist angle, providing a programmable angular degree of freedom that reshapes electronic band structures and interactions, and has enabled unconventional superconductivity,[1–3] Mott insulating states,[4] and moiré excitons.[5] Twisting simultaneously modifies the stacking point-group symmetry, thereby determining the presence or absence of inversion symmetry, which is crucial for second-harmonic generation (SHG). In the electric-dipole approximation, centrosymmetric systems yield SHG susceptibility $\chi^{(2)} = 0$, whereas non-centrosymmetric 2D crystals like monolayer transition metal dichalcogenides (TMDs) naturally host strong $\chi^{(2)}$. Therefore, SHG can serve as a sensitive probe of symmetry, enabling the detection of material characteristics such as structure and strain.[6,7] Moreover, the strong light-matter interaction in monolayer TMDs typically renders their $\chi^{(2)}$ significantly larger than that of common bulk nonlinear crystals such as $LiNbO_3$.[8–10] The integration of TMDs with existing integrated photonic platforms also holds great promise.[11]

In twisted stacks, the non-coupled limit of coherent superposition is widely used. When interlayer interaction is weak, the overall SHG response can be approximated as the coherent sum of the intrinsic monolayer $\chi^{(2)}$ tensors, with amplitude and angular dependence governed by the relative layer orientation and phase.[12] Recent theoretical calculations further show that in twisted homobilayer TMDs, where each layer is intrinsically SHG-active, strong interlayer coupling induces level repulsion, reduces the joint density of states (JDOS), and thereby suppresses the net SHG.[13] Recent experiments at $\theta < 10^\circ$ observe total SHG below the coherent-sum upper bound, corroborating this suppression.[14] By contrast, for vdW heterostructures built from SHG-silent constituents, interfacial charge transfer (CT) can create interlayer charge imbalance that breaks inversion symmetry and yields emergent SHG with magnitudes comparable to monolayer TMDs.[15,16] The SHG in vdW homostructures constructed from SHG-silent constituents has been reported in previous studies.[17,18] However, these studies primarily analyze the phenomenon from the perspective of overall symmetry and lack more microscopic-level insight. For such vdW homostructures built from SHG-silent components, whether a similar charge-imbalance-induced effect can occur remains unexplored.

Here, we address how interlayer coupling in a homostructure composed of SHG-silent constituents can both permit and tune a second-order response. We focus on twisted monolayer-bilayer graphene ($t(1+2)$LG). As illustrated in Fig. 1(a), isolated monolayer graphene (1LG) and bilayer graphene (2LG) are SHG-silent in the electric-dipole limit,

†Corresponding author. E-mail: liuzb@nankai.edu.cn

© 2026 Chinese Physical Society and IOP Publishing Ltd. All rights, including for text and data mining, AI training, and similar technologies, are reserved.

whereas their twisted stack $t(1+2)$LG exhibits strong SHG. First-principles calculations show that interlayer coupling induces an interlayer charge imbalance within the bilayer, which breaks inversion symmetry and thereby activates an in-plane electric dipole. This mechanism extends naturally to twisted monolayer-multilayer graphene, $t(1+n)$LG ($n = 3, 4$), and is consistent with our observations in $t(1+3)$LG and $t(1+4)$LG. Notably, the SHG intensity of $t(1+2)$LG can exceed that of monolayer WS_2, despite the latter's large $\chi^{(2)}$, underscoring the efficiency of the response. Our results establish SHG as a sensitive probe of interlayer coupling and charge redistribution. They also delineate a pathway distinct from CT-driven "emergent SHG" in heterostructures: in graphene homostructures, coupling-induced internal charge redistribution is the core mechanism that breaks inversion and activates $\chi^{(2)}$, with generalizability to other homostructure platforms.

To fabricate $t(1+2)$LG, we employed the standard dry transfer method.[19] First, we used hexagonal boron nitride (hBN) to separate the tightly bound 1LG and 2LG. 1LG was first lifted, followed by the rotation of 2LG by a specific angle, and then transferred to a new fused quartz substrate. On the fused quartz substrate, a monolayer WS_2 was pre-exfoliated using the mechanical exfoliation method, which served as a reference material for SHG calibration. We performed Raman characterization using a WITec Alpha 300RAS confocal Raman system with an excitation laser at 532 nm. The SHG setup consisted of a home-built optical platform excited by a Yb-doped fiber laser (Menlo Systems; 1040 nm center wavelength, 100 MHz repetition rate). The standard test power for SHG is 4.3 mW. The emitted second-harmonic signal was recorded using an iHR320 spectrometer (HORIBA Scientific).

The charge difference density was calculated using the Vienna *Ab initio* Simulation Package (VASP) based on density functional theory (DFT), employing the Perdew–Burke–Ernzerhof (PBE) functional and the projector augmented-wave (PAW) method.[20–22] A plane-wave cutoff energy of 600 eV was used. Structural relaxation was performed until the forces on all atoms were less than 10^{-8} eV/Å. A $9\times9\times1$ k-point mesh was used for structural relaxation, and a $15\times15\times1$ mesh was adopted for self-consistent field (SCF) calculations. The van der Waals interactions between layers were described using the DFT-D3 method of Grimme.[23]

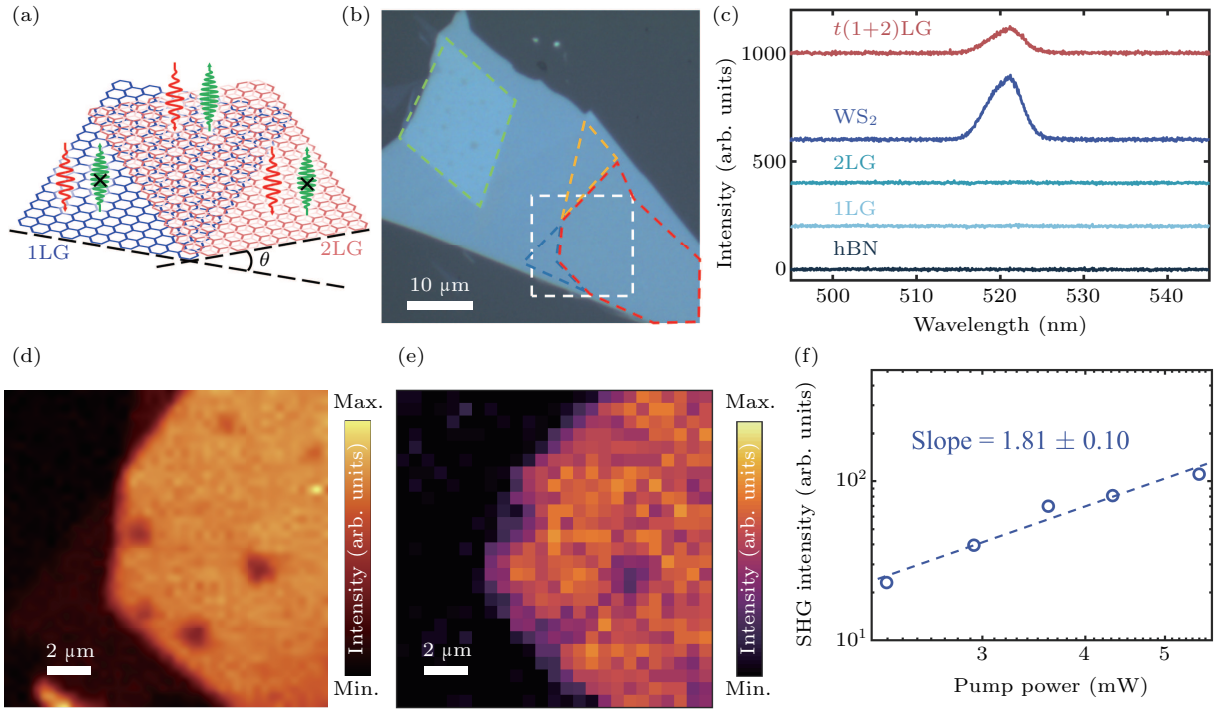


Fig. 1. Structure and SHG in $t(1+2)$LG. (a) Schematic of twisted monolayer–bilayer graphene showing the pump and its second-harmonic; inversion-symmetric regions are SHG-silent. (b) Optical micrograph showing monolayer graphene (outlined in yellow), bilayer graphene (outlined in blue), $t(1+2)$LG (outlined in red), and a 1L-WS_2 flake (outlined in green) serving as a reference for second-harmonic generation (SHG) measurements. Scale bar, 10 μm. (c) SHG spectra with a pronounced peak at the second harmonic of the pump, $t(1+2)$LG (red solid line), reaches a magnitude comparable to 1L-WS_2 (blue solid line). However, no SHG was observed in 2LG (cyan solid line), 1LG (light blue solid line), or hBN (black solid line). (d) Raman G-integrated map of the white box in the optical micrograph. Scale bar, 2 μm. (e) SHG map of the white box in the optical micrograph. Scale bar, 2 μm. (f) The log–log plot of the SHG intensity from the $t(1+2)$LG as a function of the pump laser power.

The optical image of the sample is shown in Fig. 1(b), where the red box marks the $t(1+2)$LG region, the orange box marks the 2LG region, the dark blue box marks the 1LG region, and the green box represents the WS_2 calibration region. The sample was placed on a home-built SHG optical setup, with a numerical aperture of 0.42 in the objective lens, ensuring that we were detecting SHG induced by in-plane polarization. In Fig. 1(c), no SHG was observed in hBN because

we used even-layered hBN. Additionally, SHG was not detected in 1LG or 2LG due to their centrosymmetric structures. However, a prominent peak at 520 nm is observed in the SHG spectrum from the $t(1+2)$LG region, corresponding to half the pump wavelength of 1040 nm, indicating a strong SHG response. ABA-stacked trilayer graphene has been reported to exhibit relatively strong SHG.[24] However, it remains nearly two orders of magnitude weaker than that of $t(1+2)$LG (see Fig. S7). To quantify the SHG intensity of $t(1+2)$LG, we used 1L WS_2 as a comparison material, finding that the SHG responses from $t(1+2)$LG and WS_2 are of the same order of magnitude. This suggests that $t(1+2)$LG far surpasses the weak in-plane polarization of $t(1+1)$LG,[17] in agreement with results from Song *et al.*[18] In Fig. 1(c), the ultrafast photoluminescence from graphene is absent due to its extremely weak intensity, which can only be detected under higher excitation power (see Fig. S5).[25] Further structural analysis was carried out using Raman mapping, with the G-peak integrated intensity scan shown in Fig. 1(d). The Raman data reveal the uniformity of the $t(1+2)$LG region, clearly distinguishing it from other regions. Additionally, we performed SHG mapping, with a step size of 600 nm, and the results at 520 nm are shown in Fig. 1(e). No SHG was detected in the 2LG region, consistent with its D_{3d} point group symmetry, which possesses inversion symmetry and results in $\chi^{(2)}=0$. Strong SHG was only observed in the $t(1+2)$LG region. Since monolayer and bilayer graphene exhibit no SHG signal, SHG arising from factors such as substrate doping can be ruled out. Figure 1(f) shows the power dependence of SHG in $t(1+2)$LG. The SHG intensity follows a near quadratic relationship with the pump power, with a slope close to 2, further confirming that this is almost a SHG process. Although 1LG and 2LG exhibit inversion symmetry, according to the interference superposition theory for uncoupled layers,[12] no SHG should be generated when they are stacked. However, the observed strong SHG in $t(1+2)$LG indicates that interlayer coupling between 1LG and 2LG occurs, leading to a novel nonlinear optical effect.

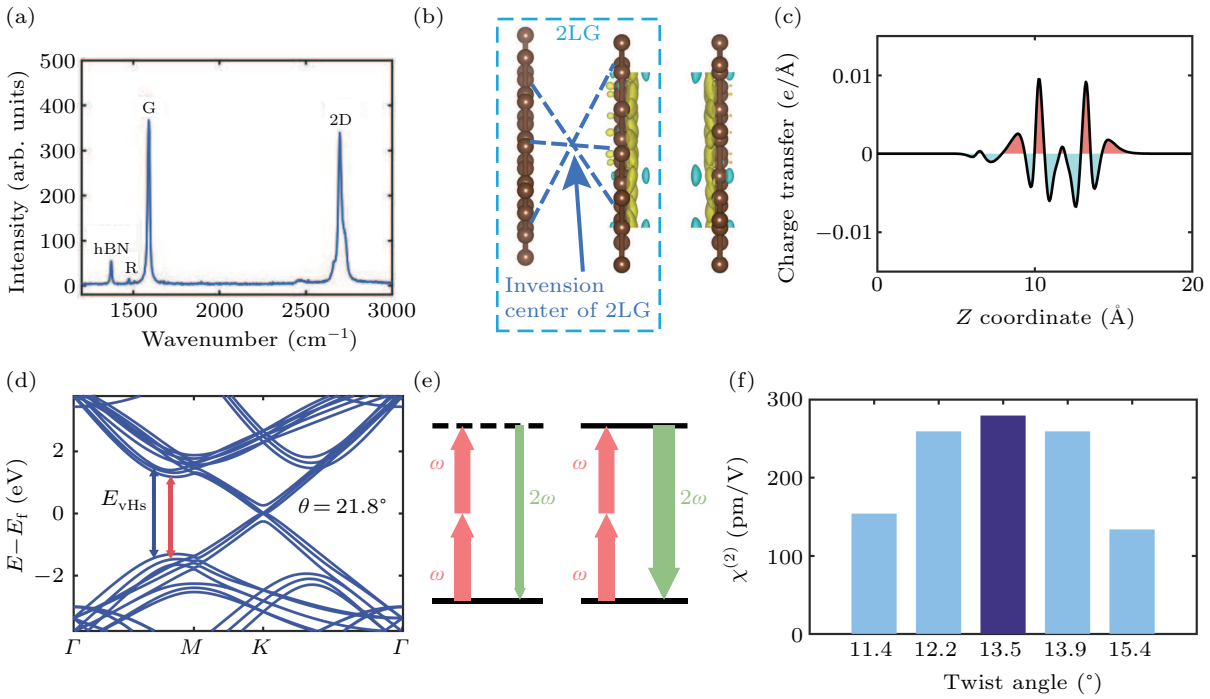


Fig. 2. Differential charge density, symmetry breaking, and resonance-enabled SHG. (a) Raman spectroscopy of a $t(1+2)$LG sample. (b) Differential charge density of $t(1+2)$LG. The isosurface is 5×10^{-5} e/Å^3. The yellow and blue regions represent the accumulation and depletion of electrons, respectively. (c) Plane-averaged differential charge density of $t(1+2)$LG. (d) and (e) Band structure with van Hove singularities and a schematic of the two-photon SHG pathway; resonance with a vHs enhances the nonlinear response. (f) $\chi^{(2)}(\theta)$ determined by referencing on-chip 1L-WS_2.

Interlayer coupling between the monolayer and the underlying bilayer in $t(1+2)$LG is first identified by Raman measurements. Under 532 nm excitation (Fig. 2(a)), a pronounced R mode appears near the G band at 1466.7 cm^{-1}, which uniquely fixes the twist angle at $\theta=15.4°$ and confirms the presence of interlayer coupling.[26] The feature at $\sim$ 1366 cm^{-1} originates from hBN and is not a graphene defect peak, excluding defect-related artifacts. To uncover the microscopic origin of the strong SHG observed in Fig. 1, we computed the differential charge density using first-principles theory. A commensurate supercell at $\theta=21.78°$ was employed to reveal mechanisms rather than to fit absolute magnitudes. The isosurfaces in Fig. 2(b) show pronounced interlayer charge imbalance within AB-2LG: electrons accumulate in the interface-proximal layer ("near" layer) and deplete from the far layer. With respect to the geometric inver-

sion center of AB-2LG, the differential charge density distribution is no longer symmetric, indicating that inversion symmetry is removed inside the bilayer. Plane averaging along z (Fig. 2(c)) yields layer-resolved net charges (in e/cell), $\Delta q_{\text{near}} = +1.1466 \times 10^{-3}$, $\Delta q_{\text{far}} = -8.6747 \times 10^{-4}$, $\Delta q_{\text{SLG}} = -2.8603 \times 10^{-4}$, with the total $\Delta q_{\text{all}} = -6.875 \times 10^{-6}$ (charge conservation within numerical tolerance). Interfacial coupling also induces a finite charge imbalance in 1LG, but electric-dipole-allowed SHG is insensitive to C_n rotation symmetry operation with $n > 3$;[27] hence, 1LG itself is not expected to radiate appreciable SHG. The permitted second-order response therefore arises from inversion removal within AB-2LG.

The calculated band structure at $\theta = 21.78°$ (Fig. 2(d)) exhibits clear van Hove singularities (vHs) near the M point, which substantially enhance the joint density of states. As sketched in Fig. 2(e), off-resonant SHG proceeds via a virtual intermediate state and is intrinsically weak; when $2\hbar\omega$ approaches a real transition associated with a vHs, the energy denominator is reduced and two-photon resonance strongly amplifies $\chi^{(2)}$. This "permission + resonance" framework predicts that tuning the twist angle, and thus the twist-angle-dependent energy difference between conduction and valence vHs (E_{vHs}), should modulate $\chi^{(2)}$. We verified this by fabricating $t(1+2)$LG devices with different twist angles and extracting $\chi^{(2)}(\theta)$ under identical optics via intensity referencing to on-chip monolayer WS_2. The resulting $\chi^{(2)}$ in Fig. 2(f) shows a clear non-monotonic angle dependence with a maximum of 279.4 pm/V near $\theta = 13.5°$, where $2\hbar\omega$ matches the vHs-related transition energy (detailed discussion can be found in supplementary information S12),[28] yielding the strongest SHG. Altogether, strong SHG in $t(1+2)$LG is consistently explained by an interfacial-coupling-induced interlayer charge imbalance that removes inversion symmetry inside AB-2LG (activating the electric-dipole), followed by two-photon resonance at the vHs that amplifies the response.

To further test that interlayer charge imbalance removes inversion symmetry and thereby activates SHG, we perform polarization-resolved measurements. In Fig. 3, we use the SHG angular response to determine the allowed tensor components and the in-plane crystal orientation. The sample is kept fixed while only the incident linear polarization is rotated by an angle α, the detection channel uses a fixed vertical analyzer. Interlayer coupling lowers the symmetry of the AB-2LG from D_{3d} to C_{3v}. The C_{3v} symmetry results in non-zero in-plane and out-of-plane second-order nonlinear susceptibilities. Incident light polarized along the x-direction allows for a nonzero in-plane electric polarization. Under this geometry, the SHG intensity follows $I^{2\omega} = \left(\chi^{(2)}_{yyy} \cos(2\alpha - 3\theta_x)\right)^2$, where θ_x encodes the in-plane crystal orientation relative to the laboratory x axis. Because of the $\cos^2(2\alpha)$, the measured polar plots exhibit a four-lobed pattern. When compared with the on-chip monolayer WS_2 reference, the $t(1+2)$LG curves show the same functional form but a phase offset arising from the different in-plane orientations. These observations are consistent with Fig. 2, where inversion symmetry is lifted in AB-2LG by interfacial coupling, and they offer an independent means to determine the crystal orientation from polarization measurements.

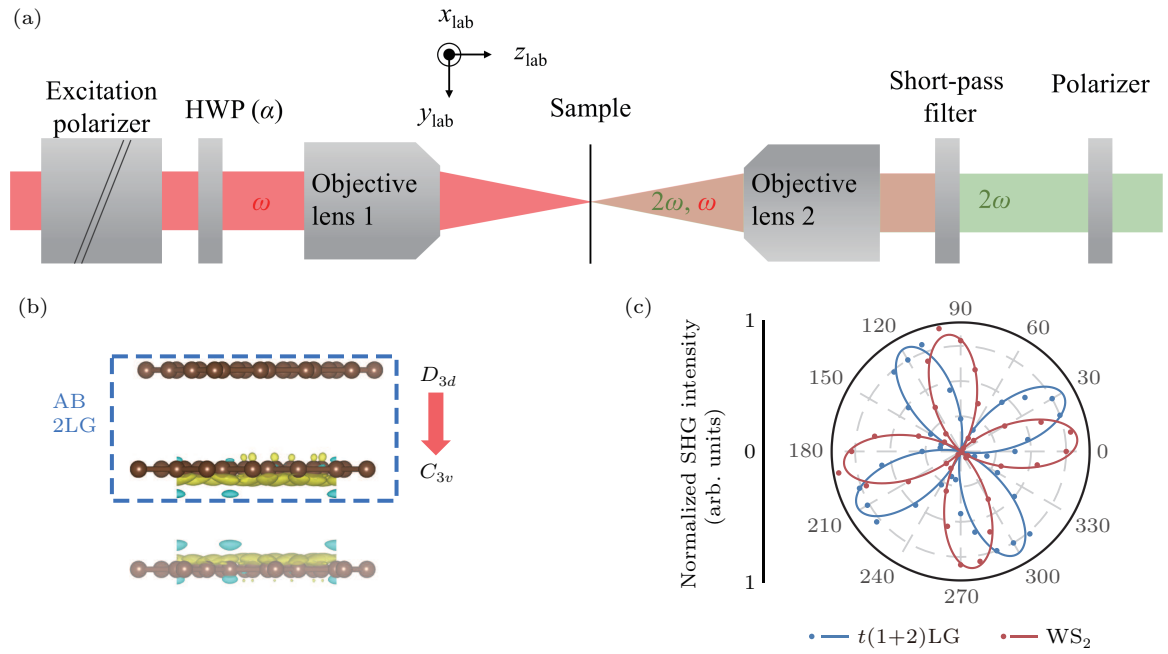


Fig. 3. Polarization-resolved patterns of SHG intensity in a fixed-analyzer geometry. (a) Transmission setup: the incident polarization is rotated while the sample is fixed, and the analyzer is fixed along the y-axis. (b) Interlayer coupling lowers the symmetry of the lower stack from D_{3d} to C_{3v}, activating the in-plane electric dipole. (c) Normalized polarization-dependent SHG from $t(1+2)$LG and the WS_2 reference.

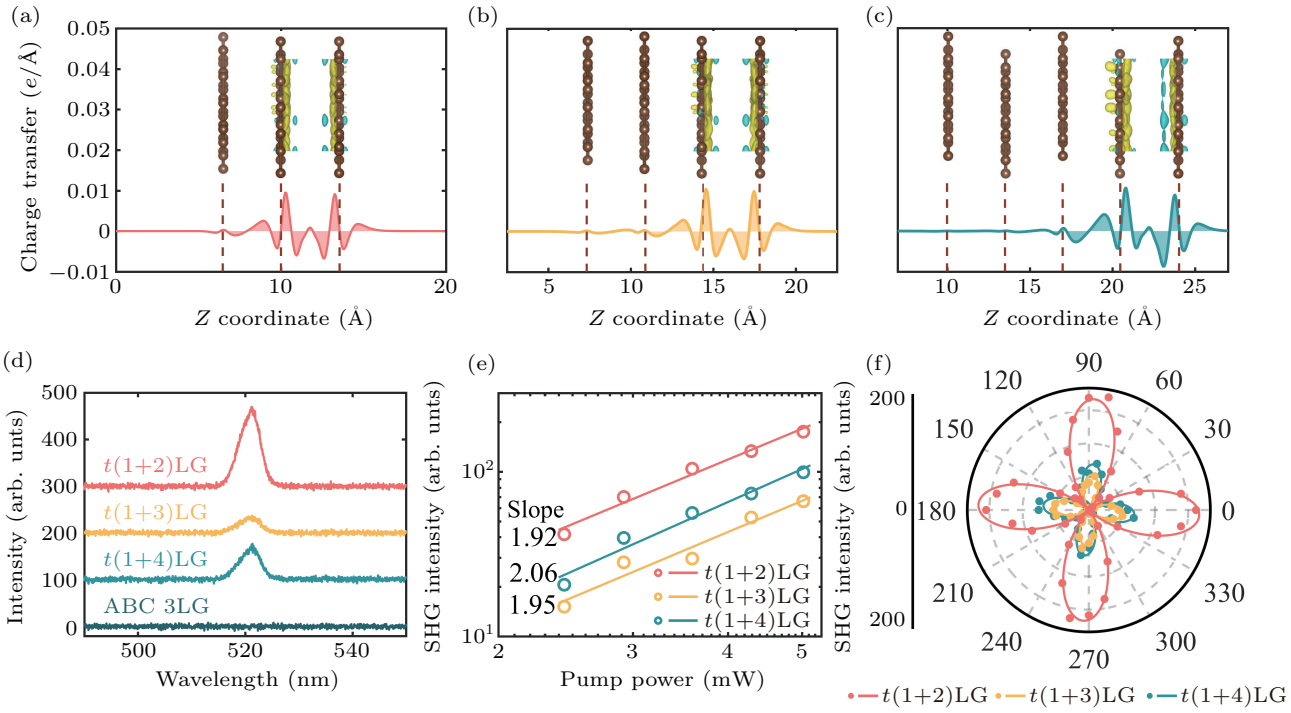


Fig. 4. Differential charge density and SHG in $t(1+n)$LG ($n = 2, 3, 4$). (a)–(c) Plane-averaged differential charge density for $t(1+2)$LG, $t(1+3)$LG, and $t(1+4)$LG. The insets show the corresponding three-dimensional charge density difference with an isosurface level of 5×10^{-5} e/Å^3. (d) SHG spectra from $t(1+n)$LG ($n = 2, 3, 4$) and ABC-3LG. (e) The log–log plot of the SHG intensity from the $t(1+n)$LG ($n = 2, 3, 4$) as a function of the pump laser power. (f) Polarization-resolved SHG from $t(1+n)$LG ($n = 2, 3, 4$).

To test the generality of the mechanism established in Fig. 2, we extend the differential charge density analysis to twisted monolayer–multilayer graphene, $t(1+n)$LG, with $n = 2, 3, 4$. Figures 4(a)–4(c) present the plane-averaged profiles (main panels) alongside three-dimensional isosurfaces (insets). In all stacks, electrons accumulate in the layer directly contacting the monolayer, while compensating depletion decays into deeper layers, an interface-proximal "polarization sheet" is evident. These observations indicate that twist-induced interlayer coupling introduces an out-of-plane layer polarization inside the multilayer, thereby removing inversion symmetry and enabling an electric dipole. In Fig. 4(b), the trilayer below is identified as ABC-3LG by Raman (see Fig. S2(b)). For $t(1+4)$LG (Fig. 4(c)), layer-resolved integration yields (in e/cell): for the three layers on the right side, $\Delta q_{\rm near} = +4.7148\times10^{-3}$, $\Delta q_{\rm far} = -2.3543\times10^{-3}$, and $\Delta q_{\rm SLG} = -2.2751\times10^{-3}$, for the two layers on the left, $\Delta q_{\rm L1} = -9.965\times10^{-5}$ and $\Delta q_{\rm L2} = +1.032\times10^{-5}$. The negative compensation is nearly equally shared by the far layer and the overlying monolayer ($|\Delta q_{\rm far}|/|\Delta q_{\rm SLG}| = 1.04$). The interfacial accumulation $\Delta q_{\rm near}$ is ~4 times larger than in $t(1+2)$LG ($\sim1.1466\times10^{-3}$ e/cell), evidencing a stronger layer polarization and a longer screening length with increasing thickness. For comparability, the computational settings follow Fig. 2.

Under identical optics (1040 nm pump), figure 4(d) compares SHG spectra. The $t(1+2)$LG, $t(1+3)$LG, and $t(1+4)$LG exhibit a clear peak at 520 nm, whereas ABC-3LG shows no discernible SHG, consistent with inversion removal versus preservation. Figure 4(e) shows the power dependence. The log–log slopes are close to 2 for all twisted stacks, confirming a second-order process. Figure 4(f) reports normalized polarization-resolved SHG with a fixed analyzer, $t(1+2)$LG (red), $t(1+3)$LG (yellow), and $t(1+4)$LG (blue) display four-lobed angular patterns that are well captured by a unified form $I^{2\omega} = \left(\chi^{(2)}_{yyy}\cos(2\alpha - 3\theta_x)\right)^2$, where α is the incident polarization angle and θ encodes the in-plane crystal orientation. The common functional dependence across $n = 2, 3, 4$ corroborates a shared C_{3v}-permitted in-plane $\chi^{(2)}$ after twist-induced coupling, in agreement with the layer-polarization mechanism established in Fig. 2.

In summary, we demonstrate that $t(1+2)$LG exhibits pronounced SHG, whereas isolated 1LG and 2LG remain SHG-silent in the electric-dipole limit. First-principles calculations reveal that interlayer coupling drives an interlayer charge imbalance within the bilayer, thereby removing inversion symmetry and activating an in-plane electric dipole. By tuning the twist angle, we observe a markedly adjustable second-order response; $\chi^{(2)}$ maximizes when the two-photon resonance approaches the vHs energy. This mechanism extends naturally to $t(1+n)$LG with $n = 3, 4$, consistent with our experimental observations in $t(1+3)$LG and $t(1+4)$LG. Notably, the $\chi^{(2)}$ of $t(1+2)$LG can approach that of monolayer WS_2, underscoring its high second-order efficiency. These results establish SHG as a sensitive probe of interlayer coupling and charge redistribution in homostructure 2D materials. They

further delineate a pathway distinct from CT-driven "emergent SHG" in heterostructures: in graphene homostructures, coupling-induced internal charge redistribution is the central mechanism that removes inversion and activates $\chi^{(2)}$. The framework is generalizable to other homostructure platforms and provides a practical strategy for symmetry engineering to elicit new physical phenomena in nominally centrosymmetric material systems.

Acknowledgments

Project supported by the National Natural Science Foundation of China (Grant Nos. 12574339, 12574457, and 12174207) and Tianjin Science and Technology Project (Grant No. 24ZXZSSS00120).

References

[1] Lu X, Stepanov P, Yang W, Xie M, Aamir M A, Das I, Urgell C, Watanabe K, Taniguchi T, Zhang G, Bachtold A, MacDonald A H and Efetov D K 2019 *Nature* **574** 653
[2] Stepanov P, Das I, Lu X, Fahimniya A, Watanabe K, Taniguchi T, Koppens F H L, Lischner J, Levitov L and Efetov D K 2020 *Nature* **583** 375
[3] Saito Y, Ge J, Watanabe K, Taniguchi T and Young A F 2020 *Nat. Phys.* **16** 926
[4] Cao Y, Fatemi V, Demir A, Fang S, Tomarken S L, Luo J Y, Sanchez-Yamagishi J D, Watanabe K, Taniguchi T, Kaxiras E, Ashoori R C and Jarillo-Herrero P 2018 *Nature* **556** 80
[5] Alexeev E M, Ruiz-Tijerina D A, Danovich M, Hamer M J, Terry D J, Nayak P K, Ahn S, Pak S, Lee J, Sohn J I, Molas M R, Koperski M, Watanabe K, Taniguchi T, Novoselov K S, Gorbachev R V, Shin H S, Fal'ko V I and Tartakovskii A I 2019 *Nature* **567** 81
[6] Zhao B J, Zhao J L and Gan X T 2024 *Chin. Phys. Lett.* **41** 104201
[7] Chen H, Li S Q, Wu Y, Bao X, Lei Z, Liu H, Xie Y, Gao J, Chen Y and Yan X 2025 *Chin. Phys. B* **34** 084206
[8] Malard L M, Alencar T V, Barboza A P M, Mak K F and De Paula A M 2013 *Phys. Rev. B* **87** 201401
[9] Ribeiro-Soares J, Janisch C, Liu Z, Elías A L, Dresselhaus M S, Terrones M, Cançado L G and Jorio A 2015 *2D Mater.* **2** 045015
[10] Song Y, Tian R, Yang J, Yin R, Zhao J and Gan X 2018 *Adv. Optical Mater.* **6** 1701334
[11] Jia X, Xu B, Luo J, Liu N, Wang Y, Zheng B, Xu W and Liu K 2025 *Chin. Phys. B* **34** 074205
[12] Hsu W T, Zhao Z A, Li L J, Chen C H, Chiu M H, Chang P S, Chou Y C and Chang W H 2014 *ACS Nano* **8** 2951
[13] Jiang X, Kang L and Huang B 2022 *Phys. Rev. B* **105** 045415
[14] Yuan Y, Liu P, Wu H, Chen H, Zheng W, Peng G, Zhu Z, Zhu M, Dai J, Qin S and Novoselov K S 2023 *ACS Nano* **17** 17897
[15] Zhang M, Han N, Zhang J, Wang J, Chen X, Zhao J and Gan X 2023 *Sci. Adv.* **9** eadf4571
[16] Wang J, Zhang M, Han N, Luo Z D, Chen X, Liu Y, Zhao J and Gan X 2023 *Adv. Optical Mater.* **11** 2202495
[17] Yang F, Song W, Meng F, Luo F, Lou S, Lin S, Gong Z, Cao J, Barnard E S, Chan E, Yang L and Yao J 2020 *Matter* **3** 1361
[18] Song G, Hong H, Ma C, Hao H, Yan S, Zhang Y, Liu K, Tong L and Zhang J 2025 *J. Am. Chem. Soc.* **147** 473
[19] Kim K, Yankowitz M, Fallahazad B, Kang S, Movva H C P, Huang S, Larentis S, Corbet C M, Taniguchi T, Watanabe K, Banerjee S K, LeRoy B J and Tutuc E 2016 *Nano Lett.* **16** 1989
[20] Kresse G and Furthmüller J 1996 *Phys. Rev. B* **54** 11169
[21] Perdew J P, Burke K and Ernzerhof M 1996 *Phys. Rev. Lett.* **77** 3865
[22] Kresse G and Joubert D 1999 *Phys. Rev. B* **59** 1758
[23] Grimme S, Antony J, Ehrlich S and Krieg H 2010 *J. Chem. Phys.* **132** 154104
[24] Shan Y, Li Y, Huang D, Tong Q, Yao W, Liu W T and Wu S 2018 *Sci. Adv.* **4** eaat0074
[25] Liu W T, Wu S W, Schuck P J, Salmeron M, Shen Y R and Wang F 2010 *Phys. Rev. B* **82** 081408
[26] Carozo V, Almeida C M, Fragneaud B, Bedê P M, Moutinho M V O, Ribeiro-Soares J, Andrade N F, Souza Filho A G, Matos M J S, Wang B, Terrones M, Capaz R B, Jorio A, Achete C A and Cançado L G 2013 *Phys. Rev. B* **88** 085401
[27] Dean J J and Van Driel H M 2009 *Appl. Phys. Lett.* **95** 261910
[28] Vela A, Moutinho M V O, Culchac F J, Venezuela P and Capaz R B 2018 *Phys. Rev. B* **98** 155135